

# Kinetic Monte Carlo Study of Li Intercalation in $\text{LiFePO}_4$

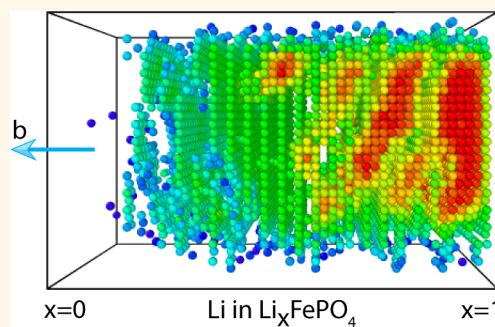
Penghao Xiao and Graeme Henkelman\*<sup>✉</sup>

Department of Chemistry and the Institute for Computational and Engineering Sciences, University of Texas at Austin, Austin, Texas 78712, United States

**ABSTRACT:** Even as a commercial cathode material,  $\text{LiFePO}_4$  remains of tremendous research interest for understanding Li intercalation dynamics. The partially lithiated material spontaneously separates into Li-poor and Li-rich phases at equilibrium. Phase segregation is a surprising property of  $\text{LiFePO}_4$  given its high measured rate capability. Previous theoretical studies, aiming to describe Li intercalation in  $\text{LiFePO}_4$ , include both atomic-scale density functional theory (DFT) calculations of static Li distributions and entire-particle-scale phase field models, based upon empirical parameters, studying the dynamics of the phase separation. Little effort has been made to bridge the gap between these two scales. In this work, DFT calculations are used to fit a cluster expansion for the basis of kinetic Monte Carlo calculations, which enables

long time scale simulations with accurate atomic interactions. This atomistic model shows how the phases evolve in  $\text{Li}_x\text{FePO}_4$  without parameters from experiments. Our simulations reveal that an ordered  $\text{Li}_{0.5}\text{FePO}_4$  phase with alternating Li-rich and Li-poor planes along the  $ac$  direction forms between the  $\text{LiFePO}_4$  and  $\text{FePO}_4$  phases, which is consistent with recent X-ray diffraction experiments showing peaks associated with an intermediate-Li phase. The calculations also help to explain a recent puzzling experiment showing that  $\text{LiFePO}_4$  particles with high aspect ratios that are narrower along the  $[100]$  direction, perpendicular to the  $[010]$  Li diffusion channels, actually have better rate capabilities. Our calculations show that lateral surfaces parallel to the Li diffusion channels, as well as other preexisting sites that bind Li weakly, are important for phase nucleation and rapid cycling performance.

**KEYWORDS:**  $\text{LiFePO}_4$ , DFT, KMC, cluster expansion, intercalation



**L** $\text{iFePO}_4$  is one of the most widely used and studied cathode materials for Li-ion batteries since it was first synthesized in Goodenough's group in 1997.<sup>1–17</sup> The material exhibits high stability, is nontoxic, and is inexpensive. Surprisingly, the rate capability of  $\text{LiFePO}_4$  is also acceptable and in fact beyond expectations for two reasons. First,  $\text{LiFePO}_4$  is an insulator, which would typically exclude it from the family of high-rate cathode materials. It is generally thought that a high-rate cathode should be an electronic conductor to facilitate transport of both  $\text{Li}^+$  ions and electrons. However, it is possible for the  $\text{Li}^+$  and  $\text{e}^-$  species to combine at the cathode surface and intercalate together as a Li atom or more specifically as a  $\text{Li}^+$  ion and an  $\text{e}^-$  polaron. As long as a  $\text{Li}^+$  ion can easily find an electron, independent of where the electron is from, electronic conductivity in the bulk cathode should not be a rate-limiting factor. One solution, carbon coating, which increases the surface electronic conductivity, was developed first with  $\text{LiFePO}_4$  and is now applied to many cathode materials. Second,  $\text{Li}_x\text{FePO}_4$  undergoes a Li-rich (LFP) and Li-poor (FP) phase separation at equilibrium. A widely accepted concept is that materials that phase separate should have low ionic diffusivity as compared to materials that accommodate a Li solid solution. Some reports, therefore, have argued that

$\text{Li}_x\text{FePO}_4$  actually follows an out-of-equilibrium solid solution pathway during rapid charge and discharge. A mechanistic understanding, however, is still lacking to explain why  $\text{LiFePO}_4$  has such a solid solution pathway while other materials do not. Such an understanding can be important for both  $\text{LiFePO}_4$  and other Li intercalation materials that phase segregate.

Recently, advanced experimental techniques have provided new insights into the intermediate phases and kinetics of  $\text{LiFePO}_4$  during charge/discharge, although discrepancies still exist due to the sensitivity for small particle sizes and other complicating experimental conditions. *In situ* (synchrotron) X-ray diffraction studies report extra peaks besides those of the LFP and FP phases. Some attribute these peaks to be a confirmation of a solid solution path, while others believe that they indicate an ordered phase between LFP and FP.<sup>12,13,17</sup> Additionally, an ordered  $\text{Li}_x\text{FePO}_4$  phase might be difficult to distinguish from a solid solution by diffraction due to similarities in the lattice parameters of the two end phases, as well as inevitable peak broadening for small particles. A

**Received:** November 22, 2017

**Accepted:** December 22, 2017

**Published:** December 22, 2017

clearly ordered phase near the composition of  $\text{Li}_{0.5}\text{FePO}_4$  with alternatively filled  $b$  channels has been observed by aberration-corrected annular bright-field scanning transmission electron microscopy.<sup>18,19</sup> Based on density functional theory (DFT) calculations, Abdellahi *et al.* have reported a detailed analysis of the chemical interfacial energies combined with the elastic energies to understand the possible Li arrangements that can be observed.<sup>20</sup> They have found that an  $ac$  interface with a diffuse solid solution region between the LFP and FP phases was of the lowest total energy, which is argued to be present at low to moderate charge/discharge rates.

With respect to the kinetics, Li *et al.* have compared the rate capabilities of  $\text{LiFePO}_4$  particles of different shapes with various exposed facet ratios.<sup>21</sup> In their experiments, particles with high aspect ratios that are narrower along the  $[100]$  direction, perpendicular to the  $[010]$  diffusion direction, can achieve higher rate capabilities. Previous calculations and experiments have confirmed that Li can easily diffuse along the  $[010]$  channels, while across the channels the barrier is prohibitively high. Fe–Li anti-site defects may allow cross-channel diffusion, but the anti-site defect concentration is measured to be low in experiments.<sup>3,9</sup> Thus, the high rate of the high aspect ratio particles cannot be explained by a shorter diffusion length; no atomistic mechanism has been proposed to account for this observation.

In this work, we have performed kinetic Monte Carlo (KMC) simulations based on DFT energetics to study the kinetics of phase evolution in  $\text{LiFePO}_4$  during charge and discharge. A cluster expansion is employed to rigorously extract the effective Li–Li interactions from hundreds of DFT calculations. Direct molecular dynamics simulations, and especially *ab initio* molecular dynamics (AIMD), are expensive and thus have limited simulation size and time. Phase field modeling can reach larger length scales and longer time scales, but it is unable to capture details at the atomic scale.<sup>22–24</sup> The approach used here extends the simulation time scale by orders of magnitude from AIMD without compromising the simulation accuracy. Our cluster expansion shows that Li–Li interactions are attractive across the  $[010]$  channels and repulsive in the same channel. KMC reveals that an ordered  $\text{Li}_{0.5}\text{FePO}_4$  phase with alternating filled and empty planes along the  $ac$  direction forms between the LFP and FP phases, which agrees with Abdellahi's analysis. The  $\text{Li}_{0.5}\text{FePO}_4$  phase forms diagonal interfaces, not parallel to any primary axis, in both LFP and FP, qualitatively agreeing with observations by synchrotron X-ray diffraction (XRD) and transmission electron microscopy (TEM).<sup>25,26</sup> Moreover, under constant voltage, particles with shorter widths along the  $a$  axis exhibit faster charge/discharge rates. The higher rate capability is due to the fact that new phases can nucleate at the  $(100)$  surface owing to missing Li–Li attractive interactions between channels at the surface. The same effect can be used to explain the defect and amorphous phase enhanced rate capability in  $\text{LiFePO}_4$ .<sup>5,6,16</sup> In all these experiments low voltage tails present in the voltage profiles indicate that some Li are weakly bound to the host structure. These weakly bound Li sites are emptied first during charge and filled last during discharge, which again reduces the Li–Li attraction between channels and facilitates nucleation.

## RESULTS

**Li–Li Interactions.** The average voltage of  $\text{LiFePO}_4$  is calculated to be 3.56 V with respect to Li metal, in agreement with experiments and other calculations.  $\text{FePO}_4$  and  $\text{LiFePO}_4$

are the only two points on the convex hull of  $\text{Li}_x\text{FePO}_4$ , but several partially lithiated structures with Li concentrations of 0.333, 0.5, 0.667, and 0.875 lie within 2 meV/f.u. (formula unit) above the hull, which have fully filled  $ac$  layers well mixed with empty layers. These structures retain a strong Li–Li attraction in the  $ac$  plane. The half-lithiated structure with every other  $bc$  plane filled has the highest energy because the Li–Li attractions along the  $a$  axis are disturbed. The above observations qualitatively agree with previous computational studies.<sup>20,27</sup> A comprehensive picture of Li–Li interactions can be gained from the largest terms in the cluster expansion.

Ten clusters are selected by minimizing the cross validation score, all of which are pairs. The geometric information and corresponding effective cluster interactions (ECIs),  $J$ , are listed in Table 1. The dominant six pairs are illustrated in Figure 1.

**Table 1. Clusters**

no.	end point	degeneracy	$J$ (meV)	radius (Å)
1	(−1, 0, −1)	4	−64	5.7
2	(−1, 1, −1)	4	−51	6.5
3	(−1, 1, 1)	4	−30	6.5
4	(−1, 2, −1)	4	−31	8.3
5	(0, 1, 0)	2	140	3.0
6	(0, 2, 0)	2	45	6.0
7	(0, 0, 2)	2	−16	4.7
8	(0, 1, 2)	4	10	5.6
9	(0, 2, 2)	2	27	7.6
10	(0, 2, −2)	2	−22	7.6

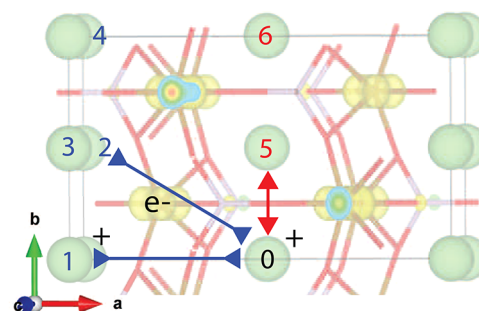


**Figure 1.** Six dominant pairs from our cluster expansion as numbered in Table 1. The red arrows and numbers indicate repulsive interactions with atom 0, and the blue ones represent attractive interactions. Green spheres are Li; red sticks are bonds connecting to O; brown sticks connect to Fe; purple sticks connect to P; yellow clouds are electrons donated from Li.

The ECI values are based on the lattice gas interpretation where the basis is chosen as  $(0, 1)$ , which means that only two sites both being occupied by Li contribute to the total energy. In this way, the ECIs directly represent interaction energies of Li–Li pairs. Based on Table 1, a Li ion attracts Li from the neighboring channels and repels Li within the same channel. The attraction stems from  $\text{Li}^+$  sharing electrons on the  $\text{Fe}^{2+}$  centers that partition the channels, which can be understood as a favorable dipole–dipole interaction between two  $(\text{Li}^+ - \text{e}^-)$  species. The strongest attraction is in the  $ac$  plane. Between the  $ac$  planes, the intrachannel repulsion and the diagonal attraction largely cancel, so that the overall interplane attraction is weak. It is the effective Li–Li attraction that leads to the phase separation, as reported in previous studies.<sup>28,29</sup>

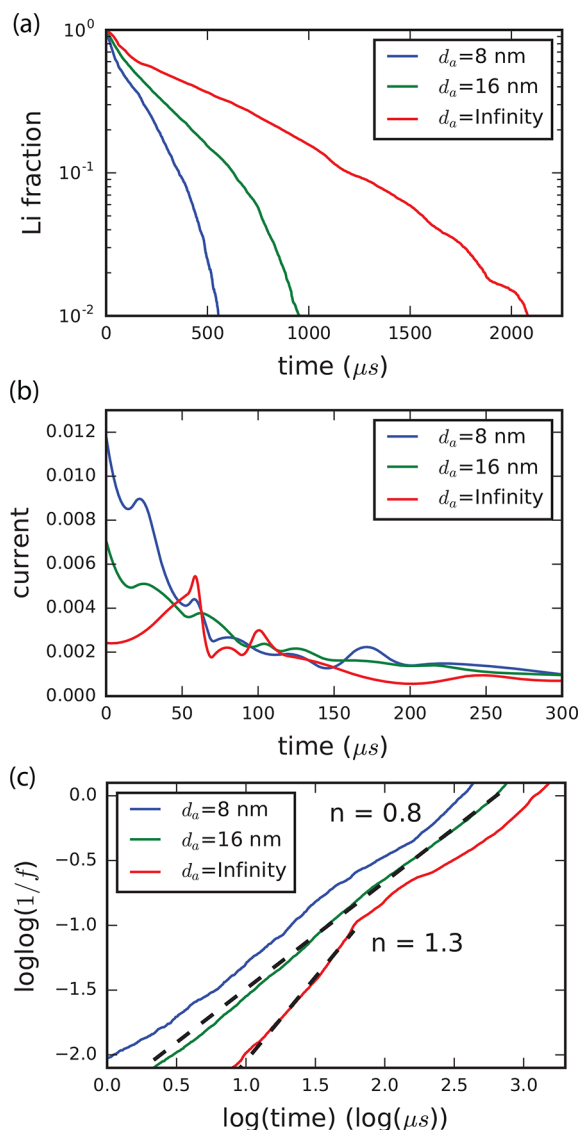
**Charge Kinetics.** Based on the above Li–Li interactions, the charge kinetics of three particles are compared using KMC simulations. The three have the same diffusion length of 15 nm (50 Li sites) along the  $b$  axis and periodic boundary conditions in the  $c$  direction. The lengths along the  $a$  direction,  $d_a$ , are 8 nm, 16 nm, and infinite, modeled with periodic boundaries. No new ECIs are introduced for surface sites; the only effect of the (100) surface is eliminating half of the attractive pairs from the neighboring columns. The charge processes are under a constant voltage of 3.80 V, 0.24 V higher than the calculated equilibrium voltage. This relatively high overpotential is needed to fully charge in the simulations within an accessible computational time. The challenge comes from the time scale difference between Li hopping in a single phase region and near the phase boundary. Li hopping is very fast in the dilute limit because few Li–Li bonds are formed or broken and the energy landscape is relatively flat. For a phase boundary parallel to the  $ac$  plane to evolve, however, the strongest Li–Li attractions in the  $ac$  plane, labeled as cluster 1 in Table 1, have to be broken to nucleate a new layer of Li. Phase boundary motion is more difficult because it requires the nucleation of a new layer sufficiently large to be as stable as the previous layer. In spite of these computational challenges, our simulations are able to reach millisecond time scales.

Figure 2(a) is a plot of the Li fraction (Li/Fe ratio) as a function of time during charge for the three particles. Figure 2(a) shows that thinner particles charge significantly faster. In contrast with the established understanding that fast charging kinetics must be a result of a short diffusion length, no Li hopping along the  $a$  axis is allowed in our simulations.<sup>2,3,9,30</sup> Here the (100) surface facilitates fast kinetics by providing nucleation sites for  $ac$  layer formation due to the fact that the surface sites are missing half of the possible Li–Li attraction between the  $b$  channels. When the overall Li concentration is below 0.02, the remaining Li are unlikely to interact, and thus the delithiation rates (slopes) of the three particles converge.

The preexisting-nucleus effect is clear in the current data shown in Figure 2(b). The current is proportional to the slope of Li fraction *vs* time. When charging starts, the thickest particle, with infinite  $d_a$ , exhibits a profound nucleation feature where the current reaches a peak at 50  $\mu$ s; the two thinner particles have higher initial currents and no significant nucleation peak. The above observation qualitatively agrees with the experimental results in ref 31; as the mean particle size decreases from 203 nm to 45 nm, the initial current increases and the current peak corresponding to nucleation disappears. It is worth noting that there are other possible nucleation sites besides the (100) surface, including defects or amorphous regions that weakly bind Li. If connected to the surface by a percolation path, these weakly bound Li sites will be depopulated first during charge and serve as nuclei in the same way as the (100) surface. The observation that many high-rate LiFePO<sub>4</sub> samples possess longer low-voltage tails, as compared to carefully crystallized materials, suggests a connection between weakly bound Li sites and fast kinetics and that facile nucleation is a plausible explanation for their high rate capabilities.<sup>5,6,16</sup>

The Kolmogorov–Johnson–Mehl–Avrami (KJMA) model<sup>32–35</sup> is often used to analyze the phase transition kinetics, where the volume fraction decay of the initial phase follows

$$f = \exp(-kt^n) \quad (1)$$



**Figure 2.** (a) Li fraction as a function of time during charge,  $f(t)$ ; (b) derivative of  $f(t)$ , which is proportional to the charging current; (c) Avrami plot where the slope gives the Avrami exponent; the upper and lower black dashed lines have a slope of 0.83 and 1.3, respectively.  $d_a$  is the particle width along the  $a$  axis.

Here  $f$  is the volume/mole fraction of the initial phase,  $t$  is time,  $k$  is the overall rate constant, and  $n$  is the Avrami exponent. From the original derivation,  $n$  is interpreted as the dimensionality of the phase growth. Experimentally obtained  $n$  values for LiFePO<sub>4</sub> are close to 1.0, suggesting a one-dimensional growth of the phase boundary.<sup>4,31,36</sup> Figure 2(c) shows the  $\log(\log(1/f))$  versus  $\log(t)$  plots from our simulations. The blue and green curves with preexisting nuclei closely follow a linear line with a slope of 0.83, not far from 1.0. For larger particles where nucleation rates are nonzero but decreasing, values of  $n$  in a range of 1.05 to 1.2 are also observed in ref 31, corresponding to the  $d_a = \infty$  case in our simulation where  $n = 1.3$ . Fortunately, given the qualitative agreement between our simulations and the experiments, we do not have to interpret the Avrami exponent to learn about the phase transformation mechanism; rather we can learn about the mechanism directly from the configurations at different states of charge in Figure 3.

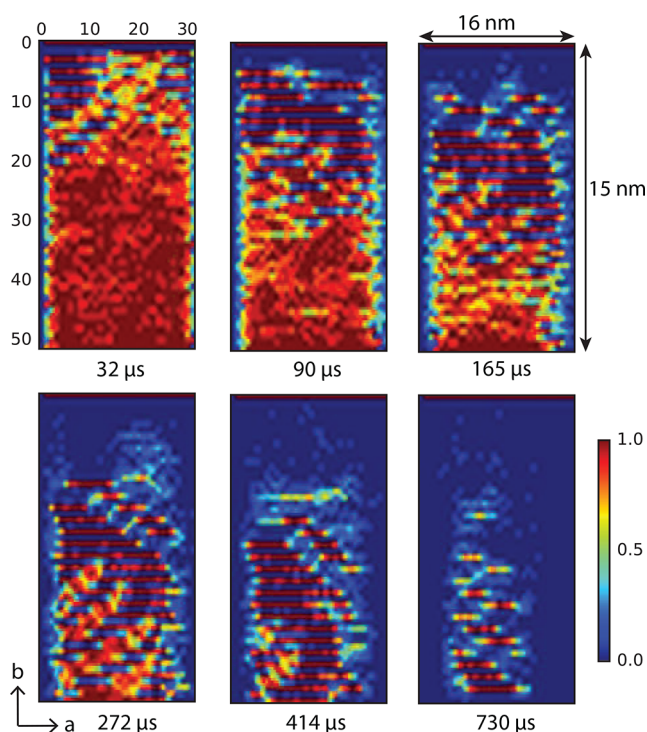


**Figure 3.** Li arrangements during charge for  $d_a = 16$  nm. The color map represents Li occupation of the  $c$  columns. The particle simulated has a rod morphology: 16 nm (32 sites) along  $a$ , 30 nm (100 sites) along  $b$ , and periodic along  $c$  with an 8 nm long unit cell (32 sites). Only half of the particle along  $b$  is explicitly simulated through the adoption of reflecting boundary conditions.

**Intermediate Phases.** Li distributions in the  $d_a = 16$  nm particle as a function of charge state are shown in Figure 3. The phase evolution remains close to a two-phase equilibrium between LFP and FP, but with a relatively wide interface at the phase boundary. The intermediate phase at the boundary has an average Li concentration near 0.5. However, it is clearly not

a solid solution, but rather an ordered structure with alternating Li-rich and Li-poor monatomic layers along the  $b$  axis. Viewing the structure along the  $b$  axis, however, as most TEM experiments have done, could lead to an incorrect conclusion that this structure is a solid solution. The simulated XRD pattern of this  $\text{Li}_{0.5}\text{FePO}_4$  phase shows intermediate peaks between FP and LFP for the (200), (211)/(020), and (301) planes, in agreement with the nascent peaks observed in *in situ* experiments.<sup>12,13</sup>

To better resolve the phase boundary propagation pattern along the  $a$  direction, supercells with twice the length along the  $a$  and  $c$  directions and shorter along the  $b$  direction were simulated. A set of configurations calculated for the delithiation process are shown in Figure 4. While the horizontal interfaces perpendicular to the  $b$  axis can be clearly seen, there are also diagonal interfaces in both FP/ $\text{Li}_{0.5}\text{FePO}_4$  and  $\text{Li}_{0.5}\text{FePO}_4$ /LFP. The  $\text{Li}_{0.5}\text{FePO}_4$ /LFP interfaces have normals aligned with the [110] or  $[-110]$  directions, forming angles near  $60^\circ$  relative to the  $a$  axis; the FP/ $\text{Li}_{0.5}\text{FePO}_4$  interfaces have a larger variation, with normals varying from  $0^\circ$  to  $60^\circ$  with respect to the  $a$  axis. These orientations agree with observations from synchrotron microbeam diffraction by Zhang *et al.*<sup>26</sup>

**Discharge.** The discharge kinetics have different features from charging, although the surface acceleration contribution remains the same. The Li fraction *vs* time curves of the three particles are shown in Figure 5, under a constant voltage of 3.2 V (an overpotential of 0.36 V). The discharge is initially extremely fast, when the Li fraction is below 0.2, and slows down as the Li concentration increases. More interestingly, the rate at the start of discharge is higher than that at the end of charge when the Li fraction is below 0.2, because the former forms a true solid solution where Li and vacancies are randomly mixed, while the latter has Li aggregated in a partially filled  $ac$  plane. The difference comes from hysteresis and is a kinetic effect.

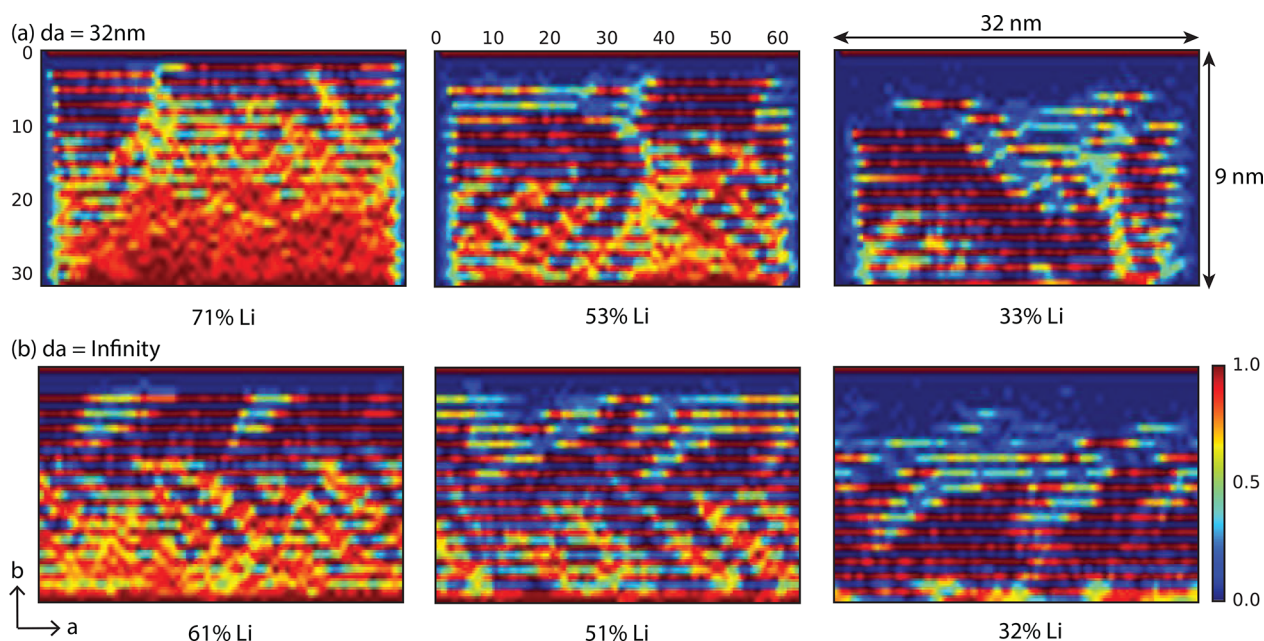


**Figure 4.** Characteristic Li configurations as a function of charge state for (a) 32 nm wide particles and (b) infinitely wide slabs.

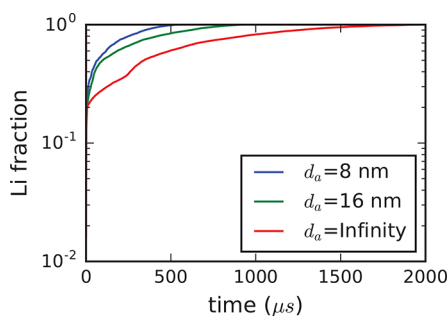


Figure 5. Li fraction as a function of time during discharge.

## DISCUSSION

The elastic energy has a profound effect on the phase evolution, as discussed in previous work.<sup>10,20,27</sup> For comparison, we have run a KMC simulation of the charging process without adding the elastic energy term. As shown in Figure 6, a

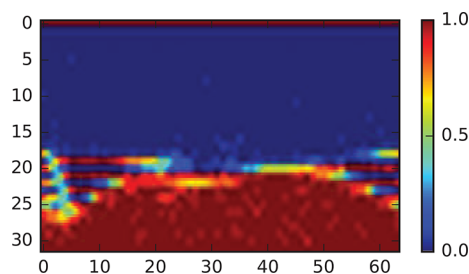


Figure 6. Li arrangements during charge without elastic energy. Periodic boundary conditions were applied along the  $a$  axis.

sharper phase boundary forms between the LFP and FP phases and the  $\text{Li}_{0.5}\text{FePO}_4$  phase shrinks to a limited region. This change is consistent with Abdellahi's previous analysis that the elastic energy causes a diffuse LFP/FP interface.<sup>20,27</sup> Moreover, without the elastic energy the delithiation time becomes an order of magnitude longer under the same voltage. The elastic energy slightly penalizes phase separation and smoothes the energy landscape, resulting in faster charge/discharge kinetics.

We should note that the absolute charge/discharge rate in our simulation is significantly faster than in experiments. Possible reasons are that our particle size is smaller than in typical experiments and also that any processes outside the cathode material are ignored, including  $\text{Li}^+$  dissolution into the electrolyte and Li interaction into the anode.

## CONCLUSIONS

A DFT-based KMC model is developed to study the phase evolution and Li intercalation kinetics in  $\text{LiFePO}_4$ . Atomistic pictures of the phase changes are obtained under realistic charge/discharge conditions. A nucleation mechanism accounting for the high-rate  $\text{LiFePO}_4$  is proposed: preexisting vacant or weakly bound sites, such as lateral surface and defects, serve as nucleation centers that facilitate the phase transition under both charge and discharge. An increase in concentration of such sites can effectively promote the rate capability of the  $\text{LiFePO}_4$  cathode.

## METHODS

**DFT.** DFT calculations were performed with the Vienna *Ab Initio* Simulation Package.<sup>37,38</sup> The Perdew–Wang-91 (PW91) functional with the Hubbard  $U$  correction was used to account for the

exchange–correlation energy.<sup>39–41</sup> An effective  $U$  value ( $U_{\text{eff}} = U - J$ ) of 4.3 eV was applied to the Fe 3d electrons.<sup>42</sup> Valence electrons were expanded in a plane wave basis set, and core electrons were described within the projector augmented wave formalism.<sup>43–46</sup> Both the atomic positions and lattice parameters were fully relaxed. A ferromagnetic spin configuration was enforced since the energetic difference with respect to an antiferromagnetic state was found to be negligible.<sup>42</sup>

**Cluster Expansion and Elastic Energy.** The cluster expansion for the Li–Li interactions was performed with the Alloy Theoretic Automated Toolkit (ATAT).<sup>47–50</sup> The training data included 241 DFT+ $U$  optimized structures and energies. To better reproduce the convex hull, points were given a weight of 10 if their formation energies per formula unit were within 2 meV/f.u. above the hull and a weight of 5 if within 20 meV/f.u. A cross validation scheme was employed to select the most significant clusters and to avoid overfitting.<sup>49</sup> The elastic energy was subtracted from the total energy of each structure for the cluster expansion, so that the cluster expansion need only describe the local energy; the elastic energy was then added back to the cluster expansion energies. While the explicit exclusion of the elastic energy to the cluster expansion changed the cluster interaction terms by only  $\sim 1$  meV, it did qualitatively affect the phase separation behavior.

The elastic energy from the lattice mismatch between the Li-rich and Li-poor phases is long-range in nature and by an order of magnitude smaller than local Li–Li interactions, and therefore it is numerically difficult to be captured by the local cluster expansion. However, a simple analytic form of the elastic energy is possible. We estimate the elastic energy per site as

$$E_{\text{elas}} = \sum_{i=1,3} \frac{1}{2} V_0 \times C_{ii}(c(r)) \times (c(r)e_{ii} - \bar{c}e_{ii})^2 \quad (2)$$

where  $V_0$  is the average volume per site;  $C_{ii}(c(r))$  are the diagonal elements of the elastic tensor;  $e_{ii}$  are the diagonal strain components between the end phases  $\text{FePO}_4$  and  $\text{LiFePO}_4$ ;  $c(r)$  is the local Li concentration at position  $r$  averaged over  $4 \times 4 \times 4$  sites; and  $\bar{c}$  is the global Li concentration averaged over the whole particle.  $C_{ii}(c(r))$  is linearly interpolated between the end point compositions,  $C_{ii}(0)$  and  $C_{ii}(1)$  are taken from calculations using the same DFT+ $U$  method described above.<sup>51</sup> In eq 2 we assume that the particle has an equilibrium strain of  $\bar{c}e_{ii}$ , and any local area that deviates from the global average concentration is compressed or stretched to accommodate the shape of the particle.  $c(r)e_{ii}$  is the intrinsic strain corresponding to the local concentration  $c(r)$ , which has no elastic energy.  $c(r)e_{ii} - \bar{c}e_{ii}$  is the deformation that the local region undergoes to conform with the particle. Equation 2 satisfies the solid solution limit where the elastic energy is zero. In a two-phase region,  $E_{\text{elas}}$  drives the Li distribution toward a solid solution in an isotropic manner.

By subtracting the elastic energy from the total energy before the fitting, the cross validation score decreases by 10% with the same clusters. The DFT-based convex hull is reproduced with the cluster expansion. Introducing the elastic energy improves the accuracy of our Hamiltonian without additional fitting parameters.

**KMC.** The rejection-free-KMC algorithm is employed to simulate the time evolution of the system. At each step, an event is selected to occur from all the possible events with a probability equal to its rate as a proportion of the total rate,  $\frac{r_i}{\sum_j r_j}$ , where  $r_i$  is the rate of event  $i$  and

$\sum_j r_j$  is the total rate. The time increment is given by  $\frac{\ln(\mu)}{\sum_j r_j}$  so that the first-escape-time distribution follows first-order kinetics with an exponential time decay. Here  $\mu$  is a uniform random number  $\in (0, 1]$ .<sup>7,52</sup>

To run KMC, barriers of Li hopping are needed to build the rate tables. Our cluster expansion is based on energies of local minima and carries no information about activation energies. By assuming a parabolic shape of the potential energy surface around a local minimum, the barrier height can be found analytically as a function of the energy difference between the initial and final state. A cartoon of

this construction is shown in Figure 7, where the saddle point is approximated by the intersection point of the two parabolas. When

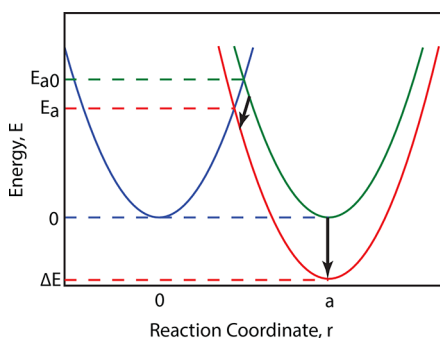


**Figure 7.** Parabolic construction showing the correlation between the energy difference of neighboring minima and the barrier height. The blue curve is the initial state,  $E = kr^2$ ; the green curve is a final state with the same energy,  $E = k(r - a)^2$ ; the red curve is a final state of lower energy,  $E = k(r - a)^2 + \Delta E$ .

the initial and final state are isoenergetic, the hopping barrier is defined as  $E_{a0}$ . If the energy of the final state is lowered by  $\Delta E$  (from the green line to the red) due to a change in the local environment, the barrier is lowered to  $E_a$ . This parabolic approximation of the potential energy surface is the same as that used in Marcus theory for calculating charge transfer rates. The positive correlation between the reaction energy and the barrier height, known as the Brønsted–Evans–Polanyi (BEP) relation, has been widely used in the field of catalysis.<sup>53–55</sup> The curvature of the parabola,  $k$ , and the distance between the two minima,  $a$ , can be combined into one variable that is determined by  $E_{a0}$ . Then,  $E_a$  is a function of  $\Delta E$ ,

$$k\left(\frac{a}{2}\right)^2 = E_{a0} \quad (3)$$

$$E_a = \frac{(4E_{a0} + \Delta E)^2}{16E_{a0}} \quad (4)$$

The evaluation of  $E_{a0}$  is based upon a single vacancy hopping in the  $\text{LiFePO}_4$  phase, which has a barrier of 0.3 eV as reported in the literature.<sup>2,9</sup> Li diffusion in  $\text{FePO}_4$  has a slightly lower barrier, which could be included in our model by making the curvature of the energy parabola a function of the Li concentration. However, for simplicity, the curvature is assumed to be constant. A linear version of eq 4 has been adopted in other KMC studies.<sup>56–58</sup> Li hopping rates were calculated within the harmonic approximation to transition state theory<sup>59</sup> using a constant prefactor of  $10^{13}$ /s.

The KMC simulation setup is shown in Figure 8. Li hops only along the  $b$  axis. One (010) surface is connected to the Li metal anode. The other end adopts a reflecting boundary condition, which effectively doubles the simulation length along  $b$ . The anode sites are always occupied so that they can supply Li as needed and at the same time are allowed to accept Li regardless of occupancy. The relative energy level of the anode is controlled by the applied voltage. In this way, the cathode (010) surface is effectively connected to a Li reservoir with the chemical potential set by the voltage. Equation 4 is also applied to calculate the barriers of Li transport from the anode to the cathode surface sites. The kinetics of  $\text{Li}^+$  diffusion in the electrolyte and deposition/detachment from the anode surfaces are assumed to be sufficiently fast to be ignored. Along the  $c$  axis, periodic boundary conditions are adopted. Along the  $a$  axis, (100) surfaces are introduced to model particles with a finite width.

## AUTHOR INFORMATION

### Corresponding Author

\*E-mail: [henkelman@utexas.edu](mailto:henkelman@utexas.edu).

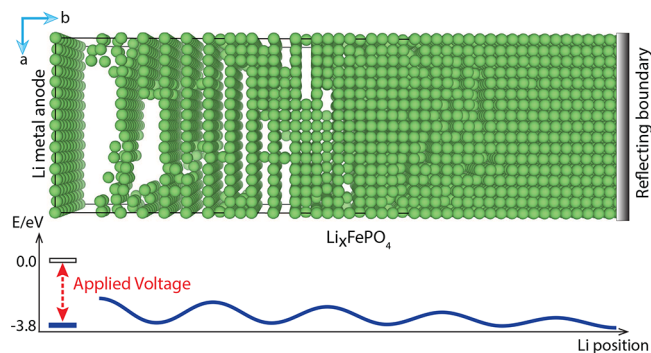


**Figure 8.** Model setup: the upper panel shows the real space configuration of Li in  $\text{Li}_x\text{FePO}_4$ ; the lower panel is a cartoon of the corresponding energy landscape. Green spheres are Li atoms. The Li arrangement shown is taken from a partial delithiation simulation.

## ORCID

Graeme Henkelman: 0000-0002-0336-7153

## Notes

The authors declare no competing financial interest.

## ACKNOWLEDGMENTS

This work was supported by the Welch Foundation (F-1841) and funds from a Peter O'Donnell Distinguished Research Award. Computational resources were provided by the Texas Advanced Computing Center.

## REFERENCES

- Padhi, A. K.; Nanjundaswamy, K.-S.; Goodenough, J. B. Phospho-olivines as Positive-electrode Materials for Rechargeable Lithium Batteries. *J. Electrochem. Soc.* **1997**, *144*, 1188–1194.
- Morgan, D.; Van der Ven, A.; Ceder, G. Li Conductivity in  $\text{Li}_x\text{MPO}_4$  (M = Mn, Fe, Co, Ni) Olivine Materials. *Electrochem. Solid-State Lett.* **2004**, *7*, A30–A32.
- Islam, M. S.; Driscoll, D. J.; Fisher, C. A.; Slater, P. R. Atomic-scale Investigation of Defects, Dopants, and Lithium Transport in the  $\text{LiFePO}_4$  Olivine-type Battery Material. *Chem. Mater.* **2005**, *17*, 5085–5092.
- Allen, J. L.; Jow, T. R.; Wolfenstine, J. Kinetic Study of the Electrochemical  $\text{FePO}_4$  To  $\text{LiFePO}_4$  Phase Transition. *Chem. Mater.* **2007**, *19*, 2108–2111.
- Gibot, P.; Casas-Cabanas, M.; Laffont, L.; Levasseur, S.; Carlach, P.; Hamelet, S.; Tarascon, J.-M.; Masquelier, C. Room-temperature Single-phase Li Insertion/extraction in Nanoscale  $\text{Li}_x\text{FePO}_4$ . *Nat. Mater.* **2008**, *7*, 741–747.
- Malik, R.; Zhou, F.; Ceder, G. Kinetics of Non-equilibrium Lithium Incorporation in  $\text{LiFePO}_4$ . *Nat. Mater.* **2011**, *10*, 587–590.
- Hin, C. Kinetic Monte Carlo Simulations of Anisotropic Lithium Intercalation into  $\text{Li}_x\text{FePO}_4$  Electrode Nanocrystals. *Adv. Funct. Mater.* **2011**, *21*, 2477–2487.
- Bai, P.; Cogswell, D. A.; Bazant, M. Z. Suppression of Phase Separation in  $\text{LiFePO}_4$  Nanoparticles During Battery Discharge. *Nano Lett.* **2011**, *11*, 4890–4896.
- Dathar, G. K. P.; Sheppard, D.; Stevenson, K. J.; Henkelman, G. Calculations of Li-ion Diffusion in Olivine Phosphates. *Chem. Mater.* **2011**, *23*, 4032–4037.
- Cogswell, D. A.; Bazant, M. Z. Coherency Strain and the Kinetics of Phase Separation in  $\text{LiFePO}_4$  Nanoparticles. *ACS Nano* **2012**, *6*, 2215–2225.
- Park, K.-S.; Xiao, P.; Kim, S.-Y.; Dylla, A.; Choi, Y.-M.; Henkelman, G.; Stevenson, K. J.; Goodenough, J. B. Enhanced Charge-transfer Kinetics by Anion Surface Modification of  $\text{LiFePO}_4$ . *Chem. Mater.* **2012**, *24*, 3212–3218.

- (12) Orikasa, Y.; Maeda, T.; Koyama, Y.; Murayama, H.; Fukuda, K.; Tanida, H.; Arai, H.; Matsubara, E.; Uchimoto, Y.; Ogumi, Z. Direct Observation of a Metastable Crystal Phase of  $\text{Li}_x\text{FePO}_4$  under Electrochemical Phase Transition. *J. Am. Chem. Soc.* **2013**, *135*, 5497–5500.
- (13) Liu, H.; Strobridge, F. C.; Borkiewicz, O. J.; Wiaderek, K. M.; Chapman, K. W.; Chupas, P. J.; Grey, C. P. Capturing Metastable Structures During High-rate Cycling of  $\text{LiFePO}_4$  Nanoparticle Electrodes. *Science* **2014**, *344*, 1252817.
- (14) Whittingham, M. S. Ultimate Limits To Intercalation Reactions for Lithium Batteries. *Chem. Rev.* **2014**, *114*, 11414–11443.
- (15) Lim, J.; Li, Y.; Alsem, D. H.; So, H.; Lee, S. C.; Bai, P.; Cogswell, D. A.; Liu, X.; Jin, N.; Yu, Y.-s.; Salmon, N. J.; Shapiro, D. A.; Bazant, M. Z.; Tylliszczak, T.; Chueh, W. C. Origin and Hysteresis of Lithium Compositional Spatiodynamics Within Battery Primary Particles. *Science* **2016**, *353*, 566–571.
- (16) Naoi, K.; Kisu, K.; Iwama, E.; Nakashima, S.; Sakai, Y.; Orikasa, Y.; Leone, P.; Dupre, N.; Brousse, T.; Rozier, P.; Naoi, W.; Simon, P. Ultrafast Charge-discharge Characteristics of a Nanosized Core-shell Structured  $\text{LiFePO}_4$  Material for Hybrid Supercapacitor Applications. *Energy Environ. Sci.* **2016**, *9*, 2143–2151.
- (17) Koyama, Y.; Uyama, T.; Orikasa, Y.; Naka, T.; Komatsu, H.; Shimoda, K.; Murayama, H.; Fukuda, K.; Arai, H.; Matsubara, E.; Uchimoto, Y.; Ogumi, Z. Two-Step Phase Transition and Competing Reaction Pathways in  $\text{LiFePO}_4$ . *Chem. Mater.* **2017**, *29*, 2855–2863.
- (18) Zhu, C.; Gu, L.; Suo, L.; Popovic, J.; Li, H.; Ikuhara, Y. Size-Dependent Staging and Phase Transition in  $\text{LiFePO}_4/\text{FePO}_4$ . *Adv. Funct. Mater.* **2014**, *24*, 312–318.
- (19) Gu, L.; Zhu, C.; Li, H.; Yu, Y.; Li, C.; Tsukimoto, S.; Maier, J.; Ikuhara, Y. Direct Observation of Lithium Staging in Partially Delithiated  $\text{LiFePO}_4$  at Atomic Resolution. *J. Am. Chem. Soc.* **2011**, *133*, 4661–4663.
- (20) Abdellahi, A.; Akyildiz, O.; Malik, R.; Thornton, K.; Ceder, G. The Thermodynamic Stability of Intermediate Solid Solutions in  $\text{LiFePO}_4$  Nanoparticles. *J. Mater. Chem. A* **2016**, *4*, 5436–5447.
- (21) Li, Z.; Peng, Z.; Zhang, H.; Hu, T.; Hu, M.; Zhu, K.; Wang, X. [100]-Oriented  $\text{LiFePO}_4$  Nanoflakes toward High Rate Li-Ion Battery Cathode. *Nano Lett.* **2016**, *16*, 795–799.
- (22) Bazant, M. Z. Theory of Chemical Kinetics and Charge Transfer Based on Nonequilibrium Thermodynamics. *Acc. Chem. Res.* **2013**, *46*, 1144–1160.
- (23) Zeng, Y.; Bazant, M. Z. Phase Separation Dynamics in Isotropic Ion-intercalation Particles. *SIAM J. Appl. Math.* **2014**, *74*, 980–1004.
- (24) Hong, L.; Liang, L.; Bhattacharyya, S.; Xing, W.; Chen, L.-Q. Anisotropic Li Intercalation in a  $\text{Li}_x\text{FePO}_4$  Nano-particle: A Spectral Smoothed Boundary Phase-field Model. *Phys. Chem. Chem. Phys.* **2016**, *18*, 9537–9543.
- (25) Mu, X.; Kobler, A.; Wang, D.; Chakravadhanula, V.; Schlabach, S.; Szabó, D.; Norby, P.; Kübel, C. Comprehensive Analysis of TEM Methods for  $\text{LiFePO}_4/\text{FePO}_4$  Phase Mapping: Spectroscopic Techniques (EFTEM, STEM-EELS) and STEM Diffraction Techniques (ACOM-TEM). *Ultramicroscopy* **2016**, *170*, 10–18.
- (26) Zhang, X.; Van Hulzen, M.; Singh, D. P.; Brownrigg, A.; Wright, J. P.; Van Dijk, N. H.; Wagemaker, M. Direct View on the Phase Evolution in Individual  $\text{LiFePO}_4$  Nanoparticles During Li-ion Battery Cycling. *Nat. Commun.* **2015**, 6.833310.1038/ncomms9333
- (27) Abdellahi, A.; Akyildiz, O.; Malik, R.; Thornton, K.; Ceder, G. Particle-Size and Morphology Dependence of the Preferred Interface Orientation in  $\text{LiFePO}_4$  Nano-Particles. *J. Mater. Chem. A* **2014**, *2*, 15437–15447.
- (28) Zhou, F.; Maxisch, T.; Ceder, G. Configurational Electronic Entropy and the Phase Diagram of Mixed-valence Oxides: The Case of  $\text{Li}_x\text{FePO}_4$ . *Phys. Rev. Lett.* **2006**, *97*, 155704.
- (29) Malik, R.; Abdellahi, A.; Ceder, G. A Critical Review of the Li Insertion Mechanisms in  $\text{LiFePO}_4$  Electrodes. *J. Electrochem. Soc.* **2013**, *160*, A3179–A3197.
- (30) Wang, L.; He, X.; Sun, W.; Wang, J.; Li, Y.; Fan, S. Crystal Orientation Tuning of  $\text{LiFePO}_4$  Nanoplates for High Rate Lithium Battery Cathode Materials. *Nano Lett.* **2012**, *12*, 5632–5636.
- (31) Oyama, G.; Yamada, Y.; Natsui, R.-i.; Nishimura, S.-i.; Yamada, A. Kinetics of Nucleation and Growth in Two-Phase Electrochemical Reaction of  $\text{Li}_x\text{FePO}_4$ . *J. Phys. Chem. C* **2012**, *116*, 7306–7311.
- (32) Avrami, M. Kinetics of Phase Change. I General Theory. *J. Chem. Phys.* **1939**, *7*, 1103–1112.
- (33) Avrami, M. Kinetics of Phase Change. II Transformation-time Relations for Random Distribution of Nuclei. *J. Chem. Phys.* **1940**, *8*, 212–224.
- (34) Avrami, M. Granulation, Phase Change, and Microstructure Kinetics of Phase Change. III. *J. Chem. Phys.* **1941**, *9*, 177–184.
- (35) Johnson, W. A.; Mehl, R. F. Reaction Kinetics in Processes of Nucleation and Growth. *Trans. AIME* **1939**, *135*, 416.
- (36) Orikasa, Y.; Maeda, T.; Koyama, Y.; Minato, T.; Murayama, H.; Fukuda, K.; Tanida, H.; Arai, H.; Matsubara, E.; Uchimoto, Y.; Ogumi, Z. Phase Transition Analysis Between  $\text{LiFePO}_4$  and  $\text{FePO}_4$  by *In-situ* Time-resolved X-ray Absorption and X-ray Diffraction. *J. Electrochem. Soc.* **2013**, *160*, A3061–A3065.
- (37) Kresse, G.; Hafner, J. *Ab initio* Molecular Dynamics for Liquid Metals. *Phys. Rev. B: Condens. Matter Mater. Phys.* **1993**, *47*, R558–R561.
- (38) Kresse, G.; Hafner, J. *Ab initio* Molecular-dynamics Simulation of the Liquid-metal Amorphous-semiconductor Transition in Germanium. *Phys. Rev. B: Condens. Matter Mater. Phys.* **1994**, *49*, 14251–14269.
- (39) Perdew, J. P. In *Electronic Structure of Solids*; Ziesche, P., Eschrig, H., Eds.; Akademie Verlag: Berlin, 1991; pp 11–20.
- (40) Perdew, J. P.; Wang, Y. Accurate and Simple Analytic Representation of the Electron-gas Correlation Energy. *Phys. Rev. B: Condens. Matter Mater. Phys.* **1992**, *45*, 13244–13249.
- (41) Dudarev, S.; Botton, G.; Savrasov, S.; Humphreys, C.; Sutton, A. Electron-energy-loss Spectra and the Structural Stability of Nickel Oxide: An LSDA+U Study. *Phys. Rev. B: Condens. Matter Mater. Phys.* **1998**, *57*, 1505–1509.
- (42) Zhou, F.; Marianetti, C.; Cococcioni, M.; Morgan, D.; Ceder, G. Phase Separation in  $\text{Li}_x\text{FePO}_4$  Induced by Correlation Effects. *Phys. Rev. B: Condens. Matter Mater. Phys.* **2004**, *69*, 201101.
- (43) Kresse, G.; Furthmüller, J. Efficient Iterative Schemes for *Ab initio* Total-energy Calculations Using a Plane-wave Basis Set. *Phys. Rev. B: Condens. Matter Mater. Phys.* **1996**, *54*, 11169–11186.
- (44) Blöchl, P. E. Projector Augmented-wave Method. *Phys. Rev. B: Condens. Matter Mater. Phys.* **1994**, *50*, 17953.
- (45) Kresse, G.; Furthmüller, J. Efficiency of *Ab-initio* Total Energy Calculations for Metals and Semiconductors Using a Plane-wave Basis set. *Comput. Mater. Sci.* **1996**, *6*, 15–50.
- (46) Kresse, G.; Joubert, J. From Ultrasoft Pseudopotentials to the Projector Augmented Wave Method. *Phys. Rev. B: Condens. Matter Mater. Phys.* **1999**, *59*, 1758.
- (47) van de Walle, A.; Asta, M. D.; Ceder, G. The Alloy Theoretic Automated Toolkit: A User Guide. *CALPHAD: Comput. Coupling Phase Diagrams Thermochem.* **2002**, *26*, 539–553.
- (48) van de Walle, A. Multicomponent Multisublattice Alloys, Nonconfigurational Entropy and Other Additions to the Alloy Theoretic Automated Toolkit. *CALPHAD: Comput. Coupling Phase Diagrams Thermochem.* **2009**, *33*, 266–278.
- (49) van de Walle, A.; Ceder, G. Automating First-Principles Phase Diagram Calculations. *J. Phase Equilib.* **2002**, *23*, 348–359.
- (50) van de Walle, A. Methods for First-Principles Alloy Thermodynamics. *JOM* **2013**, *65*, 1523–1532.
- (51) Maxisch, T.; Ceder, G. Elastic Properties of Olivine  $\text{Li}_x\text{FePO}_4$  from First Principles. *Phys. Rev. B: Condens. Matter Mater. Phys.* **2006**, *73*, 174112.
- (52) Voter, A. F. In *Radiation Effects in Solids*; Sickafus, K. E., Kotomin, E. A., Uberuaga, B. P., Eds.; Springer: Dordrecht, 2007; Vol. 235; pp 1–23.
- (53) Bronsted, J. Acid and Basic Catalysis. *Chem. Rev.* **1928**, *5*, 231–338.
- (54) Evans, M.; Polanyi, M. Inertia and Driving Force of Chemical Reactions. *Trans. Faraday Soc.* **1938**, *34*, 11–24.

(55) Bligaard, T.; Nørskov, J.; Dahl, S.; Matthiesen, J.; Christensen, C.; Sehested, J. The Brønsted-Evans-Polanyi Relation and the Volcano Curve in Heterogeneous Catalysis. *J. Catal.* **2004**, *224*, 206–217.

(56) Buendia, G. M.; Rikvold, P. A.; Park, K.; Novotny, M. Low-temperature Nucleation in a Kinetic Ising Model Under Different Stochastic Dynamics with Local Energy Barriers. *J. Chem. Phys.* **2004**, *121*, 4193–4202.

(57) Reyes, K. Fast Kinetic Monte Carlo Simulations Using Hash Table Based Caching with Applications to Nanowire Growth and Sintering. *Multiscale Model. Simul.* **2014**, *12*, 200–224.

(58) Van der Ven, A.; Ceder, G.; Asta, M.; Tapesch, P. First-principles Theory of Ionic Diffusion with Nondilute Carriers. *Phys. Rev. B: Condens. Matter Mater. Phys.* **2001**, *64*, 184307.

(59) Vineyard, G. H. Frequency Factors and Isotope Effects in Solid State Rate Processes. *J. Phys. Chem. Solids* **1957**, *3*, 121–127.